nature nanotechnology

ARTICLES

https://doi.org/10.1038/s41565-019-0493-z

Localized detection of ions and biomolecules with a force-controlled scanning nanopore microscope

Morteza Aramesh[1,2*], Csaba Forró[1], Livie Dorwling-Carter[1], Ines Lüchtefeld[1], Tilman Schlotter[1], Stephan J. Ihle[1], Ivan Shorubalko[3], Vahid Hosseini[2], Dmitry Momotenko[1], Tomaso Zambelli[1], Enrico Klotzsch[2,4] and János Vörös[1*]

Proteins, nucleic acids and ions secreted from single cells are the key signalling factors that determine the interaction of cells with their environment and the neighbouring cells. It is possible to study individual ion channels by pipette clamping, but it is difficult to dynamically monitor the activity of ion channels and transporters across the cellular membrane. Here we show that a solid-state nanopore integrated in an atomic force microscope can be used for the stochastic sensing of secreted molecules and the activity of ion channels in arbitrary locations both inside and outside a cell. The translocation of biomolecules and ions through the nanopore is observed in real time in live cells. The versatile nature of this approach allows us to detect specific biomolecules under controlled mechanical confinement and to monitor the ion-channel activities of single cells. Moreover, the nanopore microscope was used to image the surface of the nuclear membrane via high-resolution scanning ion conductance measurements.

The localized detection of ions and biomolecules is of paramount importance to understand the physics of life at the cellular and molecular scales. For example, a large number of biological processes in living cells are regulated and mediated by localized membrane transport[1]. The trafficking of macromolecules (such as proteins, RNA and DNA) and ions routed through the cell membrane determines the interaction of cells with each other, their environment and the immunological response[2]. Any dysfunction of these trafficking routes causes severe problems that lead to a variety of diseases, such as cancer and autoimmunity[3]. To understand the underlying biological mechanism of cell signalling, it is essential to identify and characterize transmembrane pathways at the single-cell level[4]. Protein secretion and/or ion-channel activities are often irregular processes and neighbouring cells within a tissue may secret significantly different amounts and/or types of proteins and/or ions in a given time[5]. Currently, there is no method for the localized detection of ionic and biomolecular pathways through the cell membrane.

Patch clamp—the gold-standard technique in studying ion channels—uses pulled glass pipettes to record the ionic current between an electrode in the pipette and one in the bath solution. The technique enables single-channel recording, but it lacks efficiency and sensitivity for protein identification[6]. Traditional methods for protein identification and characterization include mass spectroscopy, NMR spectrometry, X-ray spectroscopy, flow cytometry and immunoassays, which are impractical for time-resolved measurements of secreted proteins from single cells[5]. These obstacles significantly limit our understanding of the dynamics of the cell membrane's permeability, which is a particularly important aspect of the immunological response. The grand challenge in this field is to identify dynamically the proteins and/or ions that are secreted from a single cell into the extracellular environment. Recent methods developed for single-cell proteomics include the optical interferometric detection of scattered light from secreted proteins[5], optical imaging through molecular binding on the sensor surface[7,8] and ionic current recording using a nanopore embedded in a microfluidic incubator[9]. Despite their success and the innovative approaches, none of these techniques can be used for the localized detection of biomolecules and they lack the sensitivity to monitor ion-channel activities.

In this pilot study, we introduced a force-controlled scanning nanopore microscope that enables the localized detection of the activity of ion channels and membrane transporters by locally detecting ions and macromolecules, such as DNA and proteins. This article focuses on the fabrication and the different areas of application of this force-controlled scanning nanopore microscope in molecular biology, such as: (1) localized confinement and detection of biomolecules (for example, DNA and protein sensing), (2) extracellular recording from single cells to monitor the transmembrane activities (for example, permeation of proteins and/or ions) and (3) controlled localization of the nanopore probe into the cytoplasm and nucleus of the cell for intracellular sensing, injection and mapping of the nuclear membrane.

Detection of molecules under mechanical confinement

The platform builds on a fluid force microscope, FluidFM (Supplementary Fig. 1)[10]. The atomic force microscope (AFM) cantilevers used in this study are made of silicon nitride and contain an embedded microfluidic channel within[11]. The nanopores were fabricated via 'ion-beam sculpting'[12] using a helium ion microscope[13,14]. Briefly, the apex of the tip was flattened by ion sputtering to produce a thin film of silicon nitride (with ~$150 \times 150\,nm^2$ lateral dimensions and ~20 ± 10 nm thickness). A small hole was then fabricated in the middle of the thin film using focused He^+ ions. It is possible to shrink the pores to a desired diameter by raster

[1]Laboratory of Biosensors and Bioelectronics, Institute for Biomedical Engineering, ETH Zürich, Zürich, Switzerland. [2]Laboratory of Applied Mechanobiology, Department for Health Sciences and Technology, ETH Zürich, Zürich, Switzerland. [3]Laboratory for Transport at Nanoscale Interfaces, Swiss Federal Laboratories for Materials Science and Technology (Empa), Dübendorf, Switzerland. [4]Institute for Biology, Experimental Biophysics/Mechanobiology, Humboldt University of Berlin, Berlin, Germany. *e-mail: aramesh@biomed.ee.ethz.ch; janos.voros@biomed.ee.ethz.ch

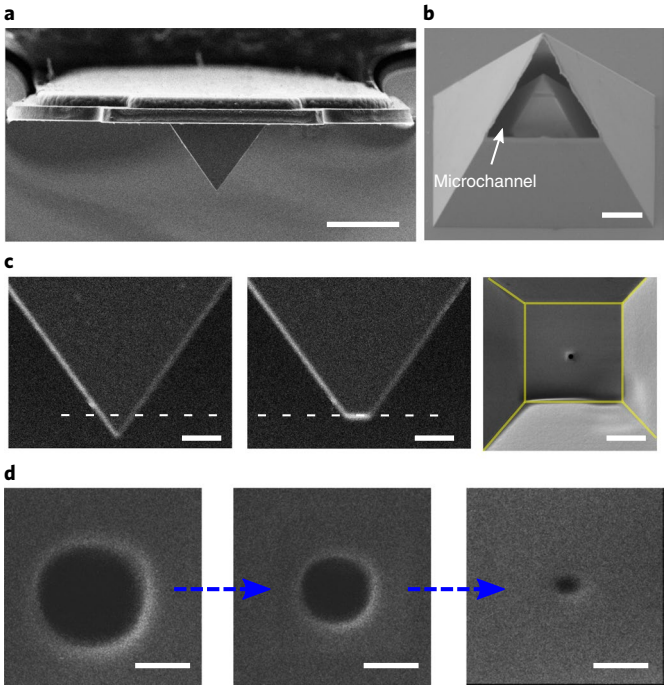

Fig. 1 | Nanopore fabrication on the AFM cantilevers. a, Scanning electron microscopy image of the cantilever at an angle perpendicular to the long axis of the cantilever. **b**, Cutaway view of a pyramidal apex with the embedded microchannel. **c**, Flattening of the pyramid apex with Ga^+ irradiation (dashed line), and the subsequent pore drilling with a focused He^+ ion beam. **d**, Example of the ion-beam sculpting process in which the prefabricated pore can be shrunk in diameter by raster scanning of He^+ ions across the pore. Scale bars, 10 µm (**a**), 1 µm (**b**), 50 nm (**c**), 20 nm (**d**).

scanning of the He^+ ions across the pore[11]. Secondary electrons produced during the fabrication process provide a simultaneous visual feedback with a high resolution (<1 nm), which allows a precise control over the pore diameter (d_{pore}) as it shrinks. Pores as small as 5 ± 1 nm in diameter were produced using this method (Fig. 1). The fabricated nanopores are similar to the conventional on-chip solid-state pores (Supplementary Fig. 2), yet they are located at the apex of AFM cantilevers. The introduced system also resembles the glass pipette pores in various aspects, such as an adaptability to scanning ion conductance microscopy[15], which can be used to image surfaces and the detection and on-demand delivery of biomolecules[16–20]. However, the AFM cantilevers are two orders of magnitude softer than glass pipettes, which allows flexibility and controlled mechanical engagement with the samples. Moreover, the wide opening angle of the fabricated pores provides a higher ionic sensitivity compared to that of the conical glass pores[21,22].

The nanopore AFM enables the nanoconfinement of biomolecules between the apex and the underlying surface. Preconfinement of biomolecules results in slower translocation speeds through the nanopore, which in general provides longer times for the sequence-based read-out[23–26]. Molecular confinement prior to the translocation also reduces the conformational variations in passing molecules by setting a barrier for the folded DNA/protein configurations[27]. Figure 2a schematically shows a situation in which the nanopore AFM generates a nanoconfined region near the surface of a glass substrate and sets a barrier for the molecules before their entrance to the nanopore. A representative current–voltage (I–V) curve for a pore near the surface and the voltage dependence of protein translocation through such a constrained geometry are shown in Fig. 2b (Supplementary Fig. 3 gives a noise analysis and Supplementary Fig. 4 gives the DNA confinement). The produced geometrical constraint at the contact with the surface limits the ionic current and therefore increases the resistance of the system. In this experiment, fibronectin (Fn) protein was introduced to the bath solution (*cis*) and a positive bias was applied to the *trans* side (the electrode was placed in the probe reservoir), which triggered (di)electrophoretic translocation of the charged proteins towards the pore. At lower voltages the protein translocation was suppressed, which suggests a reduced penetration depth of the electric field into the bulk solution and consequently a reduced capture rate of diffusing molecules. In a blank buffer solution, the number of recorded events was significantly suppressed, which confirms that the observed jumps in the current traces are due to protein translocation through the nanopore (Supplementary Fig. 5). The translocation time τ in confinement is long compared to a non-confined event, particularly evident at higher applied voltages. For example, the mean translocation time of Fn under the mechanical confinement of the AFM tip is $\sim 2.2 \pm 0.6$ ms at 400 mV in 1× PBS (note $\tau \approx 0.95 \pm 0.92$ ms at the same conditions far from the surface). However, the frequency of translocation events is lower in the confined geometry ($<5\,s^{-1}$), which implies that protein molecules encounter an energy barrier under the mechanical confinement (Supplementary Information gives a discussion on capture rates). The dynamics of the confined translocations are distinct from those with no confinement. The event duration (τ) exhibits an exponential decay with the applied voltage (V) (Fig. 2b), unlike the linear dependency observed in non-confined experiments in this study and also in other solid-state nanopore experiments[25] (but similar to the translocations observed with protein nanopores[28]). This difference can be attributed to the higher energy barrier for the translocating molecules induced by the mechanical confinement between the substrate surface and the nanopore chip. According to Kramer's theory ($\tau \approx e^{\left(\frac{\Delta G - qV}{k_B T}\right)}$), an energy barrier ($\Delta G$) can hinder the translocation of a polymer (with an effective charge q) and therefore the frictional forces between the confining surfaces and the passing molecules can alter the translocation dynamics, consistent with the friction-dominated translocation through protein nanopores[28–30]. The interaction of proteins with the probe walls can be a source of friction[31].

By increasing the set-point (SP) forces on the AFM cantilever, the distance between the nanopore and the substrate surface decreases, which is corroborated by a reduction of the background current. Correspondingly, the protein or DNA translocation time increases, which suggests the strong interaction between protein and the surfaces of the confined region. The confinement prior to translocation not only reduces the speed of biomolecules, but also more accurately determines the translocation pathways for the molecules. As a result, the standard deviation of the current transients reduces significantly (Fig. 2c). Therefore, it is concluded that the mechanical confinement of the molecules enables longer read-times for the detection which will be exploited to monitor translocation of proteins released from cells.

Extracellular mapping and detection of secreted products

Imaging of live cells using scanning probe microscopy provides a wealth of understanding about the nanoscale organization of biomolecules[32–34]. The scanning nanopore microscope enables the nanoscale monitoring of live cells using simultaneous force and ion-current feedback, which allows the generation of topographical images and the concomitant ionic current maps (Fig. 3a,b). Molecular-level cellular activities, such as protein secretion, can be monitored by the nanopore microscope through distinctive blockades and/or enhancement in the current traces (Fig. 3c).

Protein secretion from individual cells is particularly interesting and has significant importance in cellular functionality, but to monitor these proteins with nanopores requires several technical considerations. Importantly, proteins and other biomolecules tend to adsorb on the surfaces of materials within a relatively short

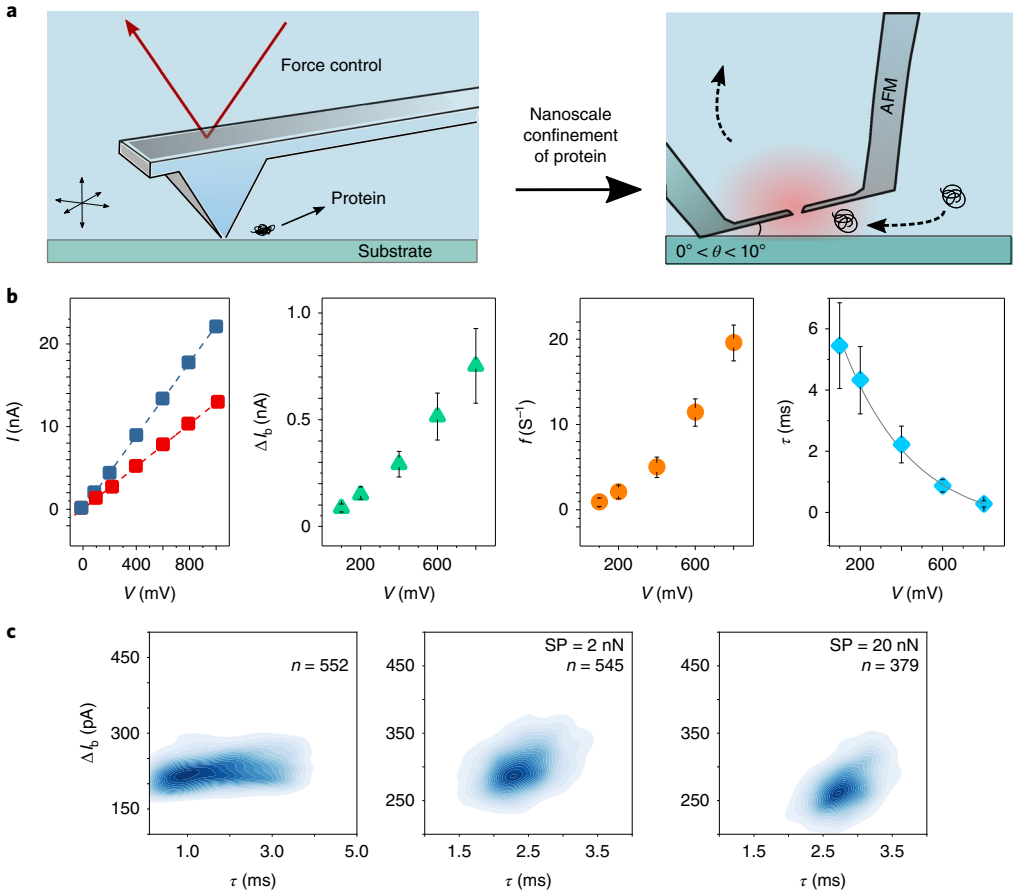

Fig. 2 | Localized detection of proteins near the surface under mechanical confinement with a nanopore AFM. a, Schematics of the experimental set-up and the concept of protein confinement using mechanical forces. The approach of the tip to the surface creates a nanoconfined area that produces an energy barrier for biomolecular translocation before the entrance to the nanopore. **b**, From left to right, the *I*–*V* curves obtained when the tip is far from the glass surface (open, $R = 45\,M\Omega$, blue curve) and near the surface (closed, $R \approx 78\,M\Omega$, red curve), the current change (ΔI_b) due to local blockage of the pore during Fn translocation, and the frequency (f) and τ of the blockage events. The voltage dependence of the Fn translocation near the surface (SP force of 2 nN) exhibits an exponential decay ($\tau \approx e^{-0.003V}$) indicative of surface interactions with the biomolecules. The error bars indicate the s.d. for each experiment. **c**, The KDE plots of the events distribution in bulk (left) and near the surface (SP = 2 nN and SP = 20 nN). The tip–surface distance (controlled by a SP force) influences the dynamics of the translocation, particularly evident from τ and the s.d. n is the number of detected events at +400 mV. d_{pore} was ~20 nm.

amount of time[35,36]. Protein adsorption on the surface of the nanopore chip was observed in our live-cell experiments, which led to a permanent blockade of the used pores within the course of a few minutes after exposure to the extracellular environment. To avoid clogging issues, the surfaces of the nanopore chips were coated with an antifouling layer using a polymer PAcrAm-g-(PMOXA, NH_2, Si) (PAcrAm, poly(2-methyl-2-oxazoline; PMOXA, poly(2-methyl-2-oxazoline))[37,38] with known protein-resistant properties. The PMOXA side chains of this molecule are 9 nm in size and are covalently bonded to the surface via the silane groups of the PAcrAm backbone. The nanopores coated with this polymer layer could be used for live-cell studies for several weeks without any permanent clogging. Figure 3c shows an example of current recorded near the surface of a cell membrane, in which several current spikes are visible during the minutes-long measurements. To make sure that the recorded current transients correspond to the cellular activity of a single cell, cells were cultured at a low density and, before the measurement, the culture medium was washed and replaced with a buffer solution without proteins (for example, PBS). In this buffer, negligible current transients were observed at distances far from the cells (for example, at a 10 µm distance) in a culture dish.

The events gathered near the outer membrane of a live cell can be attributed to the translocation of a variety of biomolecules, such as proteins or fragmented RNA/DNA, exosomes or even temporal ionic fluxes through the ion channels. These events may be distinguished by the shape of the translocation peak[39]. Proteins possess a range of charges and molecular weights, which can characteristically influence the duration and magnitude of a translocation event[39]. The nanopores exhibit a bias towards specific proteins based on their charge and molecular weights (Supplementary Fig. 6). For instance, bovine serum albumin (a negatively charged protein at pH 7.4) can be only detected at positive applied voltages, whereas lysozyme (a positively charged protein at pH 7.4) detection requires a negative applied voltage. Other proteins, such as Fn, possess a large amount of negative and positive charges on their surface and can be detected at both positive and negative voltages. The magnitude of the current change can be used for the specific detection of the biomolecules as well. For example, the magnitude of the current change is much higher for serum Fn dimers (~440 kDa) compared to smaller proteins such as bovine serum albumin (~65 kDa) and lysozyme (~15 kDa).

Classification of the peaks by their shape can also be used as a method to distinguish the source of an event. For example, a correlation

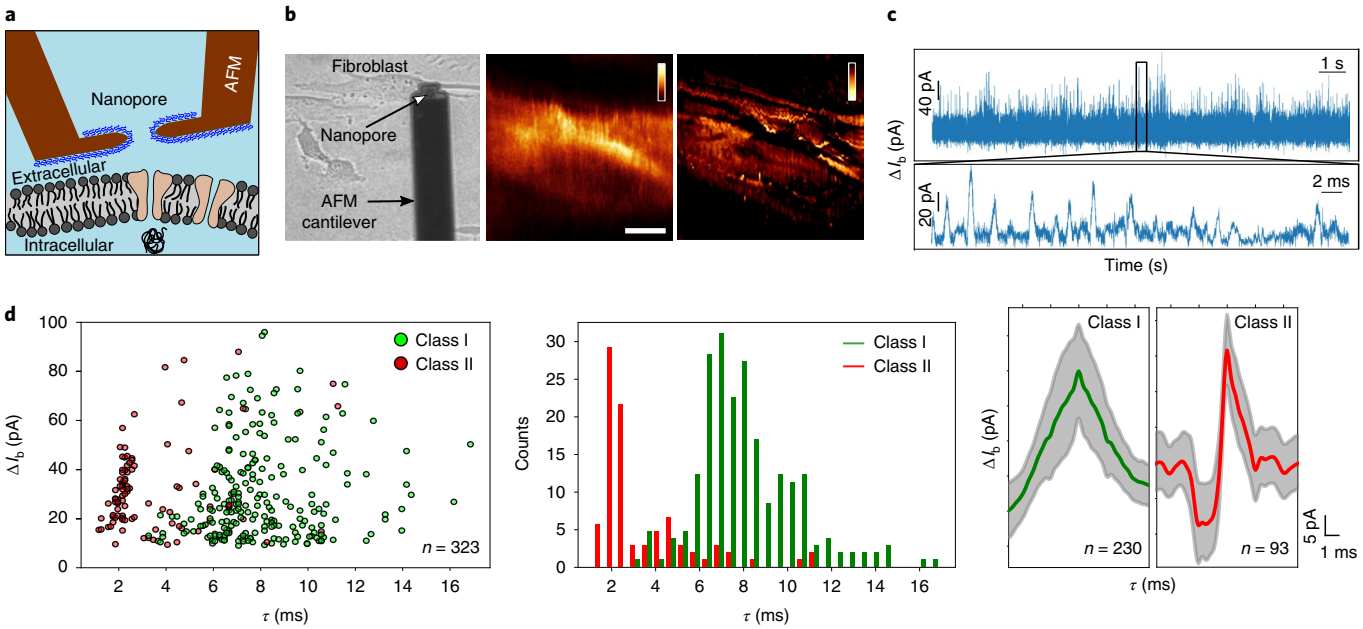

Fig. 3 | Extracellular recording from single cells. a, Schematic of a polymer-coated nanopore AFM on top of a cell membrane (it depicts the possibility of recording multiple channels and is not to scale). **b**, For the extracellular recording of protein secretion, a nanopore AFM is located on top of a fibroblast cell (left) to simultaneously record topographical (AFM feedback) (middle) and ionic current (right) maps. Scale bar, 1 μm; scale height in the AFM image, 1 μm; scale height in the current image, 100 pA). **c**, Localized detection of biomolecules and ionic fluxes on an arbitrary location on top of a fibroblast cell ($V = +100$ mV, $d_{pore} \approx 20$ nm). **d**, The scattered plot obtained from sporadic events indicates the occurrence of two significantly different types of events. Class I has a single peak profile and class II has double peaks. Each detected peak was aligned on its maximum value and sampled over time intervals of equal length. The shaded areas represent the standard deviation of the current at each sampled time point, thus representing the variation band of the peak.

clustering algorithm (Louvain method[40]) was used to analyse the current transients obtained from multiple single cells (Fig. 3d). Two significantly distinct types of events were observed in all the measurements: (1) One type of event exhibited a single-step peak in the current transient, which has a shape correlation with the blockade events acquired from pure protein solutions. (2) The second class of the current transient consists of a current reduction followed by an immediate enhancement before reaching the background level (this is not observed in pure protein solutions).

To distinguish between various types of proteins in a crowded environment of secreted products, we examined the Fn secretion of mouse embryonic fibroblast knockout for Fn (MEF $Fn^{-/-}$) versus MEF $Fn^{+/+}$ (Fig. 4). Fn is one of the major components of the extracellular matrix of fibroblasts and is expressed and assembled into a fibrillar structure in the early stage of extracellular matrix formation[41]. As MEF $Fn^{-/-}$ cells are unable to secret Fn, it can be used as a control to see if Fn can be specifically detected in MEF $Fn^{+/+}$.

The secreted products of MEF $Fn^{-/-}$ versus MEF $Fn^{+/+}$ are compared by Kernel density estimate (KDE) plots of the events distribution (Fig. 4 and Supplementary Fig. 7). The difference in the density plots of the events is particularly evident at the region with a higher current change where one would expect to detect larger biomolecules, such as Fn. As the major difference of MEF $Fn^{-/-}$ to MEF $Fn^{+/+}$ is the lack of Fn secretion, the increased density of the events at a particular region of the KDE plot in MEF $Fn^{+/+}$ is most probably due to Fn secretion of the cells.

To confirm further that the increased cell secrotome in MEF $Fn^{+/+}$ is related to Fn release, translocation of the purified Fn solution was tested with the same nanopore (Supplementary Fig. 7). The results indicated an accumulation of events in the density plots in a similar region to that where the difference between MEF $Fn^{-/-}$ and MEF $Fn^{+/+}$ is the most significant. There are minor differences in density plots of the pure Fn solution and the cell secrotome, which most probably originate from variations in the conformation of the proteins in native and purified states[42], or other physical differences in the experimental set-up, such as the interfaces of the confined regions.

Localized detection of ion channels

The working principle of nanopore sensors is based on temporal changes of ionic current and/or potential within (or nearby) the pore. Therefore, ion-channel activities in the cell membrane are expected to produce a signal in a nanopore system. As a proof-of-principle of the application of nanopores to monitor the ion-channel activities of single cells, the action potentials of individual hippocampal neuron cells were recorded (Supplementary Fig. 8). Interestingly, the recorded events during neuron 'firing' exhibit similarities to the shape of the class II current transient (Fig. 3d). Class II events were not observed in pure protein solutions. However, during the extracellular recording from live cells, this class of events were observed even at a 0 mV applied bias, at which little contribution from biomolecular translocation is expected. Therefore, the class II events can be attributed to the temporal changes of current and/or potential in the vicinity of the cell membrane, most probably due to ion-channel activities.

To demonstrate further the capability of nanopores in the localized detection of ion channels, we acquired average-current maps for the cells with a controlled number of ion channels (Fig. 5a). HEK293 with overexpressing Piezo1 ion channels or with knockout Piezo1 ion channels were used. Overexpressing cells were generated by transient transfection and the knockout cells were obtained using CRISPR/Cas9. The number of Piezo1 ion channels in the overexpressing cells was five times higher than that of the normal cells, and far more than that of the knockout cells. A nanopore was

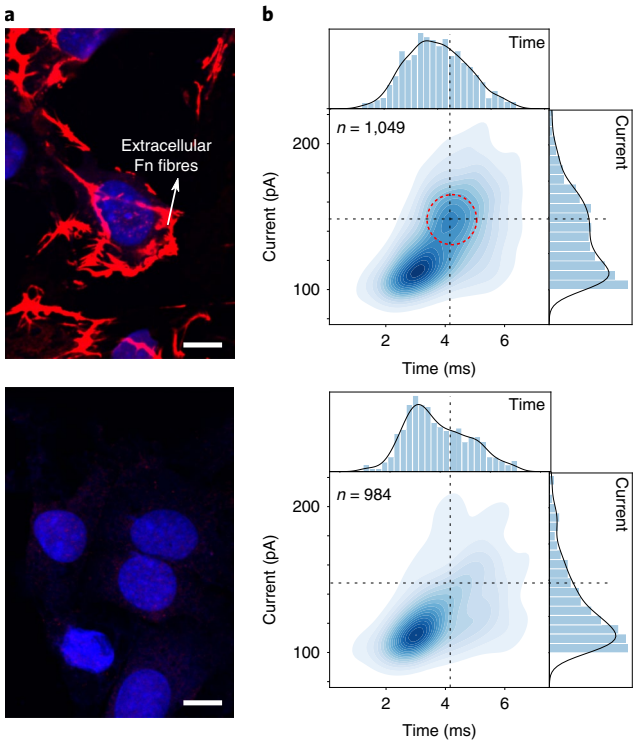

Fig. 4 | Extracellular recording from MEFs with and without Fn expression. **a**, Confocal images of fixed cells that express Fn (MEF $Fn^{+/+}$) (top image) and fixed cells that are knocked out for Fn expression (MEF $Fn^{-/-}$) (bottom image). The cell nuclei are stained in blue with DAPI (4,6-diamidino-2-phenylindole), and the Fn component of the extracellular matrix is stained in red with antibody immunostaining. Scale bars, 10 µm. **b**, Exemplary density plots of the event distribution that compare the secrotome of the cells with or without Fn expression. The current traces were recorded at +200 mV ($d_{pore} \approx 20$ nm). The increased density of the events distribution in the KDE plot of $Fn^{+/+}$ is shown by a red dashed circle, which is mostly due to Fn expression, and it is comparable with the signals obtained in pure Fn solutions. (Note: small events are excluded here.)

positioned over an arbitrary location on the cell and it was scanned over a small area ($3 \times 3\,\mu m^2$, with a 2 nN SP force in contact mode). It is evident from the recorded current maps that the cells with an excess of ion channels exhibit an abundancy of 'hot' regions (with currents higher than the background current). Particularly, as is shown in Fig. 5b, the ratio of class II/class I events is generally higher for the cells with an excess of ion channels compared to the knockout cells. These data suggest that the ion-channel activity of single cells can be monitored with the nanopore microscope in a 'loose' patch configuration (that is, with the probe positioned in close contact to the cell surface without gigaseal formation). However, at present we cannot decide whether or not it is possible to record single ion channels using this technique. The nanopore is very sensitive to minor changes in the ionic flux, which means the activities of the neighbouring channels may influence the recording. Given that the dimension of the nanopore tips ($150 \times 150\,nm^2$) is much bigger than the size of the ion channels (<10 nm) and also considering ion-channel clustering[43], the likelihood of measuring multiple neighbouring ion channels under the nanopore probe is plausible. It is anticipated that the strongest signals are correlated with the activities of the nearest channels to the probe, but contribution from neighbouring channels and from cell membrane movements cannot be excluded.

Intracellular recording, mapping and injection

Finally, we assessed the feasibility of intracellular recording using both the ionic current and the force deflection feedback (Fig. 6). By monitoring the force feedback in single-cell studies, the nanopore microscope enables intracellular recordings at particular parts of the target cells. Figure 6a shows typical force and current curves acquired during probe insertion into the cell and the subsequent withdrawal. The force feedback is related to the interaction between the nanopore tip and the cell. Four distinct instants are indicated in this curve and can be associated with the following steps: (1) the penetration of the tip through the outer cell membrane (and the nuclear membrane), (2) maintaining the set point and resting at the contact point, (3) withdrawal from the contact point and then (4) from the cell. Optical images suggest that the tip insertion inside the cell did not result in any observable change

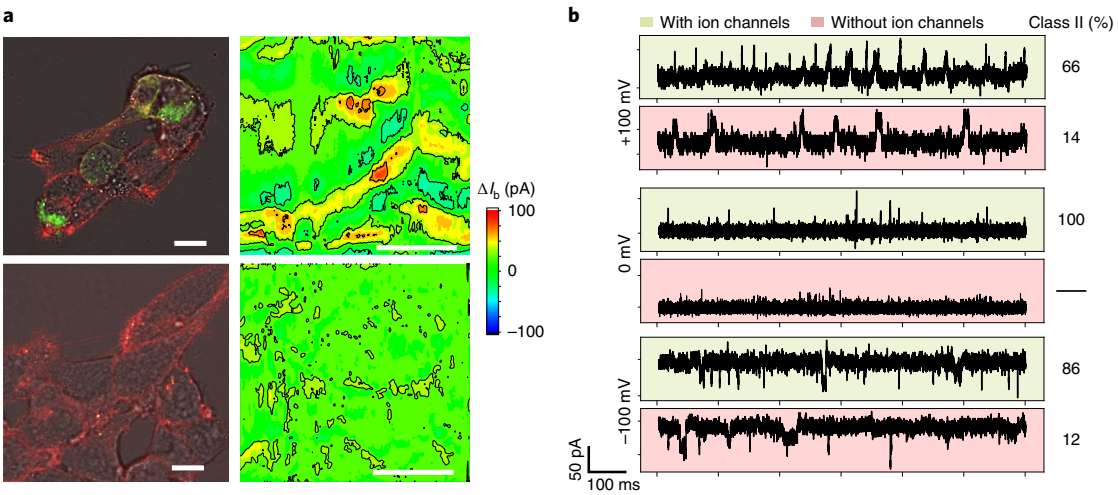

Fig. 5 | Current maps for the cells with a controlled number of ion channels and the ratio of class II to class I events. **a**, Confocal images of HEK cells (left) with overexpressing Piezo1 ion channels (top) and HEK cells with knocked-out Piezo1 ion channels (bottom). Scale bar, 20 µm. The green colour is from green fluorescent protein molecules that are specifically bound to the corresponding ion channels, and the red colour is the cell membrane tagged with Vybrant DiI cell-labelling solution. The corresponding ion-current maps (integrated over 10 ms) from HEK cells (right) with (top) and without (bottom) excess of the ion channels. (The left and right images were taken from different samples.) Scale bars, 1 µm. The probability of observing 'hot' regions (increased current changes) is higher for the cells with an excess of ion channels ($d_{pore} \approx 20$ nm). **b**, Comparison at different applied voltages of the sporadic current events near the cell membrane for the HEK cells (with an excess and with a lack of ion channels). The number of class II events (shown by percentage) is higher for the cells with more ion channels.

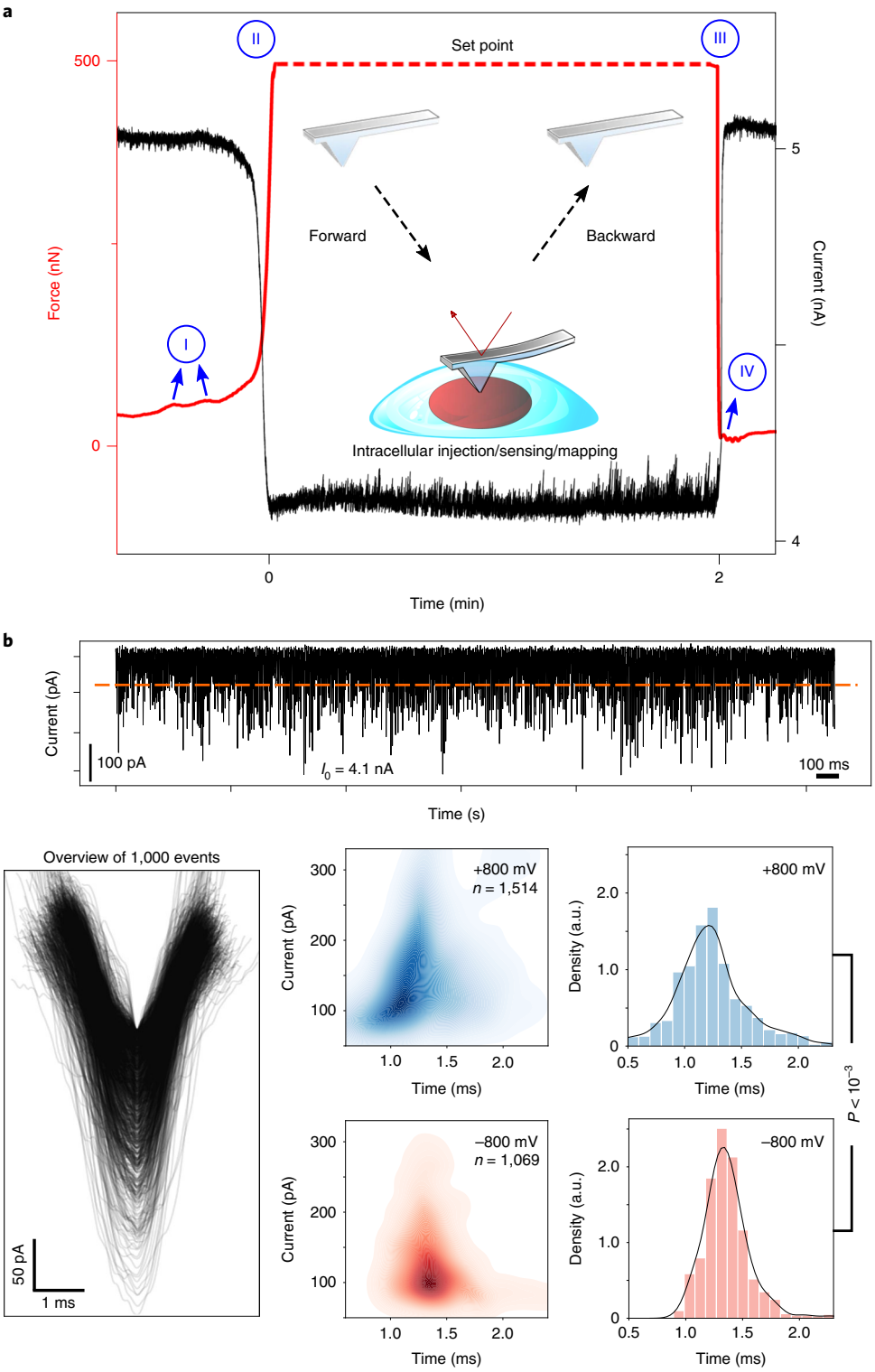

Fig. 6 | Intracellular recording with nanopore AFM. a, Laser deflection from the AFM cantilever reveals a mechanical engagement of the tip with different compartments of the cell. In a typical force-spectroscopy experiment, four distinct areas can be observed at sufficiently high SP forces (typically >300 nN). These areas are interpreted as: (I) the penetration of the tip through the cell and then nuclear membranes, (II to III) the resting time at the SP value and (IV) the retraction of the tip from the nucleus and then the cell membranes. The corresponding simultaneous current recorded during the tip insertion inside the cell is shown. The reduction of the current between (I) and (II) is due to the approach of the tip from the bulk to the surface of the cell membrane (that is, increased resistance). Similarly, the current increases back to the initial value during the withdrawal stage (III to IV). **b**, Demonstration of the intracellular monitoring of biomolecules inside a single cell (HEK). The current transients due to the nanoconfined molecular translocations through the nanopore near the surface of the nuclear membrane are shown at two different voltages ($d_{pore} \approx 20$, SP force = 500 nN and $V = \pm 800$ mV; the red line is the detection threshold, which can be decided arbitrarily). The density plots of the events are shown for the threshold value of 75 pA. *P* value was assessed with a one-way analysis of variance test.

in the cellular activity (Supplementary Fig. 9 and Guillaume-Gentil et al.[44]). After several measurements, it was found that penetration through the HEK cell membrane occurs at a force >100 nN, whereas penetration through the nuclear membrane requires forces >300 nN. By taking an intermediate value for the set point (for example, 150–250 nN), the tip can penetrate the cell membrane and stay in contact with the nucleus without further penetration. The precise insertion of the nanopore on top of the nucleus led us to directly obtain the current maps of the nuclear membrane, as shown in Supplementary Fig. 10. The current leakage through the cell membrane enabled the circuit functionality for ion-flux recording inside the cytoplasm. The intracellular sensing can be done similarly to the extracellular recording. Once the nanopore was placed near the surface of the basal or apical nuclear membrane, a large number of current spikes were observed, which are most probably due to the translocation of intracellular elements through the nanopore (Fig. 6b). Although the precise characterization of the interior contents of the cells requires additional considerations, the technique can provide statistical information on many stochastic events in different cells, and therefore enable single-cell analysis in heterogeneous cell populations. As shown here and in other studies[45], voltage control can be used for a better statistical classification of the events due to the sensitivity of the biomolecules to the applied bias. Although we are not able to determine specific types of the intracellular molecules at this stage, it is envisioned that selectivity can be achieved by functionalizing the nanopores[46], molecular tagging[47] and antibody labelling[48], or with complementary methods, such as mass spectrometry[49], post qPCR amplification[23] and the implementation of learning algorithms in data analysis[50].

Conclusions

The demonstrated concept for the realization of an AFM-controlled scanning nanopore microscope features several advantages. The use of an AFM cantilever to control the location of the nanopore makes the approach directly applicable to localized sensing of biomolecules. A nanoconfinement can be readily produced to mechanically control the translocation of the molecules prior to their entrance to the nanopore. With this approach, the speed of molecular translocations reduces significantly, as well as the standard deviation in the current transients. Also, the extracellular signalling of single cells can be monitored by recording the activity of their ion channels and counting the amount of proteins secreted by the cell, based on stochastic translocation analysis. The spatial organization of the ion channels and membrane transporters can be visualized by scanning the nanopore tip over the cell membrane while recording transient current events. Voltage control can further improve the quantitative assessment of such activities by enabling a better classification of the events. The laser deflection from the cantilever provides a sensitive feedback for the precise positioning of the nanopore inside the cell, which enables intracellular sensing and mapping at different locations, such as outer membrane, in the cytoplasm, on the nuclear membrane or inside the nucleus. As an application, the ion conductance image indicative of nanoscale features in the nuclear membrane of a living cell was obtained.

Reporting Summary. Further information on research design is available in the Nature Research Reporting Summary linked to this article.

Data availability

All the data needed to evaluate the conclusions in the paper are present in the paper. Additional data and other findings of this study are available from the corresponding authors upon reasonable request.

Online content

Any methods, additional references, Nature Research reporting summaries, source data, statements of code and data availability and associated accession codes are available at https://doi.org/10.1038/s41565-019-0493-z.

Received: 2 November 2018; Accepted: 3 June 2019;

References

1. Alberts, B., Johnson, A., Lewis, J., Raff, M., Roberts, K., Walter, P. *Molecular Biology of the Cell* (Garland Science, 2009).
2. Kollmannsberger, P., Bidan, C. M., Dunlop, J. W. C., Fratzl, P. & Vogel, V. Tensile forces drive a reversible fibroblast-to-myofibroblast transition during tissue growth in engineered clefts. *Sci. Adv.* **4**, eaao4881 (2018).
3. Catterall, W. A. From ionic currents to molecular mechanisms: the structure and function of voltage-gated sodium channels. *Neuron* **26**, 13–25 (2000).
4. Robert, C., Hue, I., McGraw, S., Gagné, D. & Sirard, M.-A. Quantification of cyclin B1 and p34(cdc2) in bovine cumulus–oocyte complexes and expression mapping of genes involved in the cell cycle by complementary DNA macroarrays. *Biol. Reprod.* **67**, 1456–1464 (2002).
5. McDonald, M. P. et al. Visualizing single-cell secretion dynamics with single-protein sensitivity. *Nano Lett.* **18**, 513–519 (2018).
6. Actis, P. et al. Compartmental genomics in living cells revealed by single-cell nanobiopsy. *ACS Nano* **8**, 546–553 (2014).
7. Gatterdam, V. et al. Focal molography is a new method for the in situ analysis of molecular interactions in biological samples. *Nat. Nanotechnol.* **12**, 1089–1095 (2017).
8. Li, X. et al. Label-free optofluidic nanobiosensor enables real-time analysis of single-cell cytokine secretion. *Small* **14**, 1800698 (2018).
9. Kennedy, E. et al. Method for dynamically detecting secretions from single cells using a nanopore. *Nano Lett.* **18**, 4263–4272 (2018).
10. Meister, A. et al. FluidFM: combining atomic force microscopy and nanofluidics in a universal liquid delivery system for single cell applications and beyond. *Nano Lett.* **9**, 2501–2507 (2009).
11. Dorwling-Carter, L., Aramesh, M., Han, H., Zambelli, T. & Momotenko, D. Combined ion conductance and atomic force microscope for fast simultaneous topographical and surface charge imaging. *Anal. Chem.* **90**, 11453–11460 (2018).
12. Li, J. et al. Ion-beam sculpting at nanometre length scales. *Nature* **412**, 166–169 (2001).
13. Aramesh, M. Ion-beam sculpting of nanowires. *Phys. Status Solidi Rapid Res. Lett.* **12**, 1700333 (2018).
14. Aramesh, M., Mayamei, Y., Wolff, A. & Ostrikov, K. Superplastic nanoscale pore shaping by ion irradiation. *Nat. Commun.* **9**, 835 (2018).
15. Ossola, D. et al. Simultaneous scanning ion conductance microscopy and atomic force microscopy with microchanneled cantilevers. *Phys. Rev. Lett.* **115**, 238103 (2015).
16. Lan, W. J., Kubeil, C., Xiong, J. W., Bund, A. & White, H. S. Effect of surface charge on the resistive pulse waveshape during particle translocation through glass nanopores. *J. Phys. Chem. C* **118**, 2726–2734 (2014).
17. Ivanov, A. P. et al. On-demand delivery of single DNA molecules using nanopipets. *ACS Nano* **9**, 3587–3594 (2015).
18. Klausen, L. H., Fuhs, T. & Dong, M. Mapping surface charge density of lipid bilayers by quantitative surface conductivity microscopy. *Nat. Commun.* **7**, 12447 (2016).
19. Perry, D., Al Botros, R., Momotenko, D., Kinnear, S. L. & Unwin, P. R. Simultaneous nanoscale surface charge and topographical mapping. *ACS Nano* **9**, 7266–7276 (2015).
20. Freedman, K. J. et al. Nanopore sensing at ultra-low concentrations using single-molecule dielectrophoretic trapping. *Nat. Commun.* **7**, 10217 (2016).
21. Steinbock, L. J., Steinbock, J. F. & Radenovic, A. Controllable shrinking and shaping of glass nanocapillaries under electron irradiation. *Nano Lett.* **13**, 1717–1723 (2013).
22. Dorwling-Carter, L. et al. Simultaneous scanning ion conductance and atomic force microscopy with a nanopore: effect of the aperture edge on the ion current images. *J. Appl. Phys.* **124**, 174902 (2018).
23. Nadappuram, B. P. et al. Nanoscale tweezers for single-cell biopsies. *Nat. Nanotechnol.* **14**, 80 (2018).
24. Pud, S. et al. Mechanical trapping of DNA in a double-nanopore system. *Nano Lett.* **16**, 8021–8028 (2016).
25. Wanunu, M., Morrison, W., Rabin, Y., Grosberg, A. Y. & Meller, A. Electrostatic focusing of unlabelled DNA into nanoscale pores using a salt gradient. *Nat. Nanotechnol.* **5**, 160–165 (2010).
26. Feng, J. et al. Identification of single nucleotides in MoS_2 nanopores. *Nat. Nanotechnol.* **10**, 1070–1076 (2015).

27. Briggs, K. et al. DNA translocations through nanopores under nanoscale preconfinement. *Nano Lett.* **18**, 660–668 (2018).
28. Maglia, G., Restrepo, M. R., Mikhailova, E. & Bayley, H. Enhanced translocation of single DNA molecules through α-hemolysin nanopores by manipulation of internal charge. *Proc. Natl Acad. Sci. USA* **105**, 19720–19725 (2008).
29. Kasianowicz, J. J., Brandin, E., Branton, D. & Deamer, D. W. Characterization of individual polynucleotide molecules using a membrane channel. *Proc. Natl Acad. Sci. USA* **93**, 13770–13773 (1996).
30. Meller, A., Nivon, L. & Branton, D. Voltage-driven DNA translocations through a nanopore. *Phys. Rev. Lett.* **86**, 3435–3438 (2001).
31. Balme, S. et al. Influence of adsorption on proteins and amyloid detection by silicon nitride nanopore. *Langmuir* **32**, 8916–8925 (2016).
32. Toyoda, Y. et al. Genome-scale single-cell mechanical phenotyping reveals disease-related genes involved in mitotic rounding. *Nat. Commun.* **8**, 1266 (2017).
33. Klotzsch, E., Stiegler, J., Ben-Ishay, E. & Gaus, K. Do mechanical forces contribute to nanoscale membrane organisation in T cells? *Biochim. Biophys. Acta Mol. Cell Res.* **1853**, 822–829 (2015).
34. Karner, A. et al. Tuning membrane protein mobility by confinement into nanodomains. *Nat. Nanotechnol.* **12**, 260–266 (2017).
35. Aramesh, M., Shimoni, O., Ostrikov, K., Prawer, S. & Cervenka, J. Surface charge effects in protein adsorption on nanodiamonds. *Nanoscale* **7**, 5726–5736 (2015).
36. Aramesh, M., Tran, P. A., Ostrikov, K. & Prawer, S. Conformal nanocarbon coating of alumina nanocrystals for biosensing and bioimaging. *Carbon* **122**, 422–427 (2017).
37. Konradi, R., Pidhatika, B., Mühlebach, A. & Textor, M. Poly-2-methyl-2-oxazoline: a peptide-like polymer for protein-repellent surfaces. *Langmuir* **24**, 613–616 (2008).
38. Weydert, S. et al. Easy to apply polyoxazoline-based coating for precise and long-term control of neural patterns. *Langmuir* **33**, 8594–8605 (2017).
39. Yusko, E. C. et al. Real-time shape approximation and fingerprinting of single proteins using a nanopore. *Nat. Nanotechnol.* **12**, 360–367 (2017).
40. Blondel, V. D., Guillaume, Jean-Loup, Lambiotte, R. & Lefebvre, E. Fast unfolding of communities in large networks. *J. Stat. Mech. Theory Exp.* **2008**, P10008 (2008).
41. Sakai, T. et al. Plasma fibronectin supports neuronal survival and reduces brain injury following transient focal cerebral ischemia but is not essential for skin-wound healing and hemostasis. *Nat. Med.* **7**, 324–330 (2001).
42. Ruoslahti, E. Fibronectin and its receptors. *Annu. Rev. Biochem.* **57**, 375–413 (1988).
43. Gottlieb, P. A. in *Current Topics in Membranes* (ed. Gottlieb, P. A.) 1–36 (Current Topics in Membranes Vol. 79, Academic, 2017).
44. Guillaume-Gentil, O. et al. Force-controlled fluidic injection into single cell nuclei. *Small* **9**, 1904–1907 (2013).
45. Larkin, J., Henley, R. Y., Muthukumar, M., Rosenstein, J. K. & Wanunu, M. High-bandwidth protein analysis using solid-state nanopores. *Biophys. J.* **106**, 696–704 (2014).
46. Wei, R., Gatterdam, V., Wieneke, R., Tampé, R. & Rant, U. Stochastic sensing of proteins with receptor-modified solid-state nanopores. *Nat. Nanotechnol.* **7**, 257–263 (2012).
47. Bell, N. A. W. & Keyser, U. F. Digitally encoded DNA nanostructures for multiplexed, single-molecule protein sensing with nanopores. *Nat. Nanotechnol.* **11**, 645–651 (2016).
48. Ren, R. et al. Nanopore extended field-effect transistor for selective single-molecule biosensing. *Nat. Commun.* **8**, 586 (2017).
49. Guillaume-Gentil, O. et al. Tunable single-cell extraction for molecular analyses. *Cell* **166**, 506–517 (2016).
50. Misiunas, K., Ermann, N. & Keyser, U. F. QuipuNet: convolutional neural network for single-molecule nanopore sensing. *Nano Lett.* **18**, 4040–4045 (2018).

Acknowledgements

This project received funding from the European Union's Horizon 2020 research and innovation programme under the Marie Skłodowska-Curie Individual Fellowship (project reference 706930) and the Career Seed Grant from ETH Zürich (project reference 0-20440-18) to M.A. The work was partially funded by the EUROSTARS project grant E!11644. D.M. is supported by the Swiss National Science Foundation Ambizione grant PZ00P2_174217/1. I.S. is thankful to Empa for financial support and to the Swiss National Science Foundation for support in equipment procurement (R'Equip 206021_133823). This work was supported by the Human Frontiers Science Program RGY0065/2017 to E.K.

The authors acknowledge the valuable and insightful discussions with C. Frei, V. Gatterdam, O. Guillaume-Gentil and V. Vogel. We are grateful to members of our laboratories for assistance during the project. We appreciate the technical assistance from S. Wheeler. The PAcrAm-g-(PMOXA, NH_2, Si) polymer was a kind donation of SuSoS AG, Switzerland. We are grateful to the Martinac lab and M. Vassalli for valuable discussions and the provided materials. The authors acknowledge support of the Scientific Center for Optical and Electron Microscopy ScopeM of the Swiss Federal Institute of Technology ETHZ.

Author contributions

M.A. and J.V. designed the experiments. M.A., C.F., L.D.-C., I.L., T.S., S.J.I., I.S. and V.H. performed the experiments. M.A., C.F. and S.J.I. performed the statistical analysis and coding with support from J.V. All the authors discussed the results and commented on the manuscript. M.A. wrote the manuscript with support from J.V.

Competing interests

The authors declare no competing interests.

Additional information

Supplementary information is available for this paper at https://doi.org/10.1038/s41565-019-0493-z.

Reprints and permissions information is available at www.nature.com/reprints.

Correspondence and requests for materials should be addressed to M.A. or J.V.

Peer review information: *Nature Nanotechnology* thanks Sebastien Balme and other, anonymous, reviewer(s) for their contribution to the peer review of this work.

Publisher's note: Springer Nature remains neutral with regard to jurisdictional claims in published maps and institutional affiliations.

nature research

Corresponding author(s): Morteza Aramesh and János Vörös

Last updated by author(s): Jun 5, 2019

Reporting Summary

Nature Research wishes to improve the reproducibility of the work that we publish. This form provides structure for consistency and transparency in reporting. For further information on Nature Research policies, see Authors & Referees and the Editorial Policy Checklist.

Statistics

For all statistical analyses, confirm that the following items are present in the figure legend, table legend, main text, or Methods section.

n/a	Confirmed	
☐	☒	The exact sample size (*n*) for each experimental group/condition, given as a discrete number and unit of measurement
☐	☒	A statement on whether measurements were taken from distinct samples or whether the same sample was measured repeatedly
☐	☒	The statistical test(s) used AND whether they are one- or two-sided *Only common tests should be described solely by name; describe more complex techniques in the Methods section.*
☐	☒	A description of all covariates tested
☐	☒	A description of any assumptions or corrections, such as tests of normality and adjustment for multiple comparisons
☐	☒	A full description of the statistical parameters including central tendency (e.g. means) or other basic estimates (e.g. regression coefficient) AND variation (e.g. standard deviation) or associated estimates of uncertainty (e.g. confidence intervals)
☒	☐	For null hypothesis testing, the test statistic (e.g. *F*, *t*, *r*) with confidence intervals, effect sizes, degrees of freedom and *P* value noted *Give P values as exact values whenever suitable.*
☒	☐	For Bayesian analysis, information on the choice of priors and Markov chain Monte Carlo settings
☒	☐	For hierarchical and complex designs, identification of the appropriate level for tests and full reporting of outcomes
☒	☐	Estimates of effect sizes (e.g. Cohen's *d*, Pearson's *r*), indicating how they were calculated

Our web collection on statistics for biologists contains articles on many of the points above.

Software and code

Policy information about availability of computer code

Data collection	All the details for data collection is included in the experimental section in supporting information.
Data analysis	Data analysis was performed using python 2.7 , OriginPro 2017 or FIJI(ImageJ). All the details can be found in the experimental section in supporting information.

For manuscripts utilizing custom algorithms or software that are central to the research but not yet described in published literature, software must be made available to editors/reviewers. We strongly encourage code deposition in a community repository (e.g. GitHub). See the Nature Research guidelines for submitting code & software for further information.

Data

Policy information about availability of data

All manuscripts must include a data availability statement. This statement should provide the following information, where applicable:

- Accession codes, unique identifiers, or web links for publicly available datasets
- A list of figures that have associated raw data
- A description of any restrictions on data availability

All data needed to evaluate the conclusions in the paper are present in the paper. The additional data and other findings of this study are available from the corresponding authors upon reasonable request.

Field-specific reporting

Please select the one below that is the best fit for your research. If you are not sure, read the appropriate sections before making your selection.

☒ Life sciences ☐ Behavioural & social sciences ☐ Ecological, evolutionary & environmental sciences

For a reference copy of the document with all sections, see nature.com/documents/nr-reporting-summary-flat.pdf

Life sciences study design

All studies must disclose on these points even when the disclosure is negative.

Sample size	Sample size was determined by measurements over fixed time intervals.
Data exclusions	Data were only excluded for failed experiments, reasons for which included suboptimal electrical recordings.
Replication	Replicate experiments were successful.
Randomization	No randomization.
Blinding	No blinded experiment.

Reporting for specific materials, systems and methods

We require information from authors about some types of materials, experimental systems and methods used in many studies. Here, indicate whether each material, system or method listed is relevant to your study. If you are not sure if a list item applies to your research, read the appropriate section before selecting a response.

Materials & experimental systems

n/a	Involved in the study
☐	☒ Antibodies
☒	☐ Eukaryotic cell lines
☒	☐ Palaeontology
☒	☐ Animals and other organisms
☒	☐ Human research participants
☒	☐ Clinical data

Methods

n/a	Involved in the study
☒	☐ ChIP-seq
☒	☐ Flow cytometry
☒	☐ MRI-based neuroimaging

Antibodies

Antibodies used	Antibodies were only used for immunostaining. Primary rabbit polyclonal antibody against fibronectin (abcam-23750) was used. The experimental section (page 5 in supporting information) provided with manuscript contains information on all antibodies used in the study.
Validation	Validation statement on the manufacturer's website: "Antibody validation must be application-specific to be effective. To address this, we carry out quality checks via immunocytochemistry/immunofluorescence (ICC/IF), immunohistochemistry (IHC), western blot, flow cytometry, ELISA, immunoprecipitation (IP), chromatin immunoprecipitation (ChIP), and peptide array. " https://www.abcam.com/primary-antibodies/how-we-validate-our-antibodies